Check for updates

Atomically precise single-crystal structures of electrically conducting 2D metal–organic frameworks

Jin-Hu Dou[1], Maxx Q. Arguilla[1], Yi Luo[2,3], Jian Li[2,3], Weizhe Zhang[4], Lei Sun[1], Jenna L. Mancuso[5], Luming Yang[1], Tianyang Chen[1], Lucas R. Parent[6], Grigorii Skorupskii[1], Nicole J. Libretto[7], Chenyue Sun[1], Min Chieh Yang[5], Phat Vinh Dip[8], Edward J. Brignole[8], Jeffrey T. Miller[7], Jing Kong[9], Christopher H. Hendon[5], Junliang Sun[2,3 ✉] and Mircea Dincă[1 ✉]

Electrically conducting 2D metal–organic frameworks (MOFs) have attracted considerable interest, as their hexagonal 2D lattices mimic graphite and other 2D van der Waals stacked materials. However, understanding their intrinsic properties remains a challenge because their crystals are too small or of too poor quality for crystal structure determination. Here, we report atomically precise structures of a family of 2D π-conjugated MOFs derived from large single crystals of sizes up to 200 μm, allowing atomic-resolution analysis by a battery of high-resolution diffraction techniques. A designed ligand core rebalances the in-plane and out-of-plane interactions that define anisotropic crystal growth. We report two crystal structure types exhibiting analogous 2D honeycomb-like sheets but distinct packing modes and pore contents. Single-crystal electrical transport measurements distinctively demonstrate anisotropic transport normal and parallel to the π-conjugated sheets, revealing a clear correlation between absolute conductivity and the nature of the metal cation and 2D sheet packing motif.

I mparting conductivity to MOFs, previously considered as insulating materials, provides new opportunities for materials research and facilitates applications that harness both porosity and electronic delocalization in extended crystalline lattices[1–6]. The unusual combination of porosity and excellent conductivity in MOFs with 2D π-conjugation has led to the development of a variety of potential applications, ranging from batteries[7–9], supercapacitors and fuel cells[10–12] to electrocatalysts[13] and chemiresistive sensors[14]. To develop 2D π-conjugated MOFs with chemically addressable electrical properties and/or redox activities, it is important to grow large single crystals[15,16], which facilitate single-crystal electrical device fabrication and atomic-resolution structural characterization by diffraction techniques—both of which are critical for understanding how physical properties relate to structure. Nonetheless, to date, 2D MOFs with well-resolved crystal structures remain scarce[1]; most, if not all, of these MOFs can only be obtained as nanocrystalline powders that also exhibit heavily disordered interlayer stacking[3,17–19]. Typically, the structures of 2D π-conjugated MOFs cannot be determined rigorously; instead, they are simply implied by matching experimental powder X-ray diffraction (PXRD) patterns with those simulated from hypothesized models[2,20]. This status quo does not provide any information on the stacking sequence of the 2D layers or on the content of the pores. The lack of studies on single-crystal structures has significantly impaired the determination of structure–property relationships that drive the materials

discovery process and are critical for the continued development of this class of porous conductors.

Ligand design strategies for single-crystal conductive 2D MOFs

Controlling crystal growth in 2D conductive MOFs is difficult because in-plane growth (that is, growth in the *ab* plane) requires continuous formation and breakage of strong metal–ligand bonds, whereas growth normal to the covalent sheets (that is, in the *c* direction) is governed by much weaker π-stacking interactions. Because the latter are much more reversible, they usually dominate growth but are too weak to enforce long-range translational symmetry, causing severe stacking disorder. Consequently, these materials exhibit long needle- or thread-like morphology, with severely stunted in-plane growth such that the *ab* dimensions of typical MOF crystallites rarely exceed several hundred nanometres. Crystal growth in these systems is further complicated by the unusually complex chemistry. Indeed, MOFs in this class are often the result of reactions involving four components: the protonated organic ligand, a metal-ion source, a base that deprotonates the ligand in situ, and an oxidant that oxidizes the ligand in situ. Traditional strategies for controlling crystal growth in such systems involve systematically changing the reactant concentration or order of addition, or controlling the reaction temperature and time. Nevertheless, these approaches do not fundamentally alter the anisotropic growth directions of a

[1]Department of Chemistry, Massachusetts Institute of Technology, Cambridge, MA, USA. [2]College of Chemistry and Molecular Engineering, Beijing National Laboratory for Molecular Sciences, Peking University, Beijing, China. [3]Department of Materials and Environmental Chemistry, Stockholm University, Stockholm, Sweden. [4]National Facility for Protein Science, Shanghai Advanced Research Institute, Shanghai, China. [5]Material Science Institute, Department of Chemistry and Biochemistry, University of Oregon, Eugene, OR, USA. [6]University of Connecticut, Innovation Partnership Building, University of Connecticut, Storrs, CT, USA. [7]Davidson School of Chemical Engineering, Purdue University, West Lafayette, IN, USA. [8]Department of Biology, Massachusetts Institute of Technology, Cambridge, MA, USA. [9]Department of Electrical and Engineering and Computer Science, Massachusetts Institute of Technology, Cambridge, MA, USA. ✉e-mail: junliang.sun@pku.edu.cn; mdinca@mit.edu
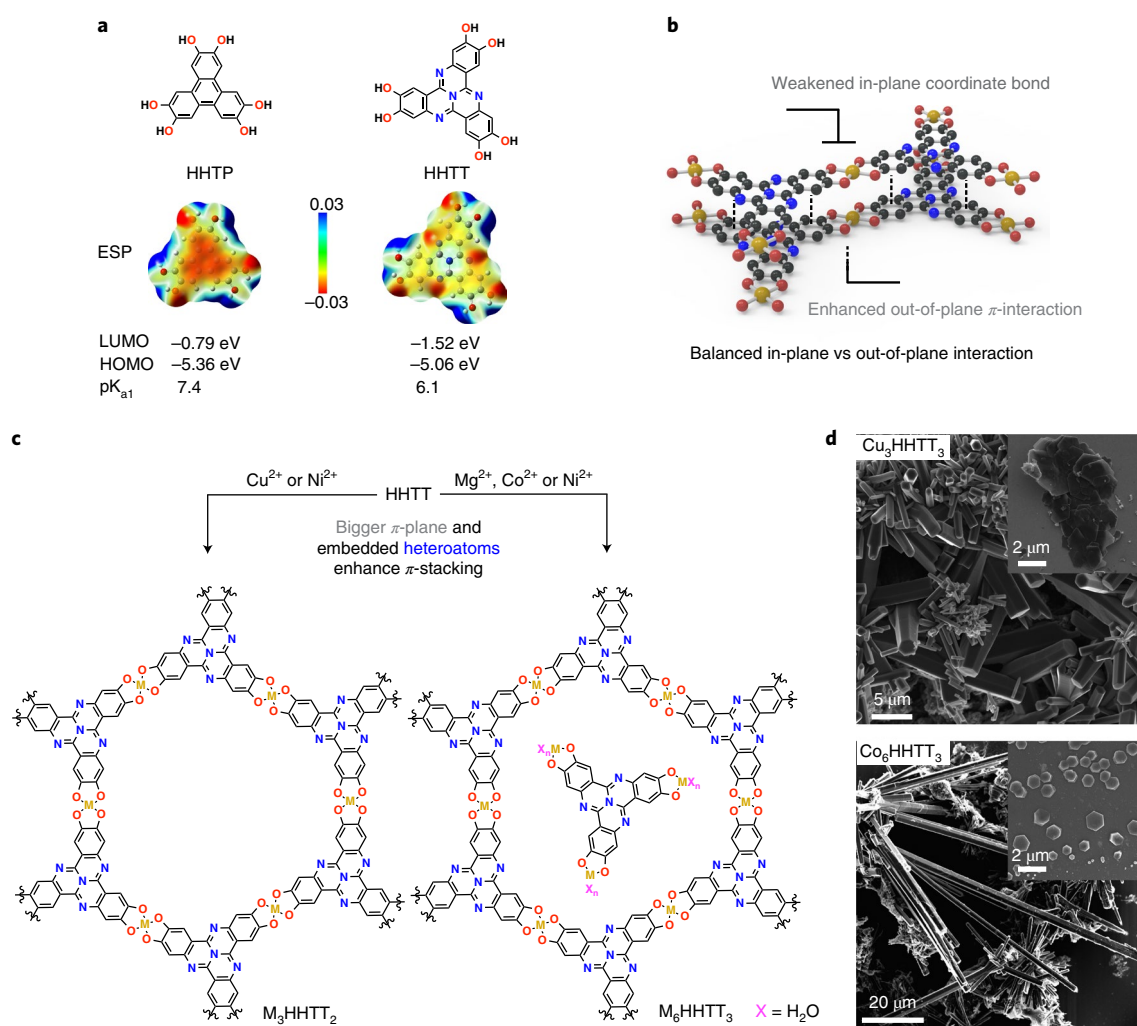
Fig. 1 | Design strategy and synthetic conditions for the growth of single crystals of 2D MOFs. a, Chemical structures of HHTP and HHTT with electrostatic potential (ESP) maps and computed pK_{a1} values. Computed energy values (referenced to vacuum) of the highest occupied molecular orbital (HOMO) and lowest unoccupied molecular orbital (LUMO) of HHTT and HHTP highlight the more electron deficient character of the former. **b**, Schematic illustration of the conductive 2D MOF stacking lattice. **c**, Molecular design strategy for creating porous and dense 2D MOFs. Axially coordinating water molecules in M$_6$HHTT$_3$ are omitted for clarity. **d**, Scanning electron microscopy (SEM) micrographs of Cu$_3$HHTT$_2$ and Co$_6$HHTT$_3$ that can be isolated on-demand with either rod- or plate-like (inset) morphology by varying the synthetic conditions (see Methods in Supplementary Information).

given crystallite and have yielded only marginal improvements in the crystal dimensions[21].

Instead of relying on these traditional methods for controlling crystal growth, we sought to fundamentally rebalance the in-plane and out-of-plane growth of conductive 2D MOFs by altering the ligand electronic structure (Fig. 1a). The molecular and electronic structure of the ligand core influences both the in-plane crystal growth, by modifying the nature of the metal–ligand bond, and the π-stacking between the 2D sheets. For this particular class of 2D conductive MOFs, we hypothesize that a large, electron-deficient ligand core with reduced electron density at the metal-binding site will increase the acidity of the metal-binding functional group, resulting in a more pronounced reversibility of the metal–ligand bond and higher in-plane crystallinity. These design principles are exemplified by the ligand 2,3,7,8,12,13-hexahydroxy tetraazanaphthotetraphene (HHTT) (Fig. 1a; see Supplementary Information for synthesis). The choice of this ligand is inspired by concepts in organic electronics, whereby enlarging the π-conjugation and embedding heteroatoms into the backbone result in stronger non-covalent interactions between adjacent molecules[22–25]. Here,

the tetraazanaphthotetraphene core features a larger π-conjugated plane than the triphenylene core (such as in 2,3,6,7,10,11-hexahydroxytriphenylene, HHTP) in archetypical 2D MOF ligands, which should favour stronger inter-ligand interactions and more ordered π-stacking, as demonstrated in closely related organic π-based systems. In addition, the three peripheral pyridinic nitrogen atoms in HHTT significantly decrease its electron density and consequently lower the energy of the lowest unoccupied molecular orbital (LUMO) relative to that of HHTP (Fig. 1a). This should increase the acidity of the catechol groups in HHTT relative to HHTP and is similar to why more acidic carboxylates yield more crystalline MOFs than less acidic triazoles and pyrazoles[26]; the former should promote higher crystallinity in the *ab* plane. Our hypothesis is further substantiated by calculations that specifically compare the pK_{a1} values of HHTP and HHTT (Fig. 1a), which predict that the latter (pK_{a1} = 6.06) is one order of magnitude more acidic than the former (pK_{a1} = 7.39). Therefore, the HHTT core should promote a higher degree of both in-plane and out-of-plane crystallinity (Fig. 1b). Further modulation of the interlayer interactions should be possible by employing different metal ions that prefer either square-planar

or octahedral coordination. The latter prefer axially coordinated solvent molecules whose hydrogen bonding interactions compete with π-stacking and facilitate additional dynamic crystallization to limit crystal defects[27]. We optimized and investigated the three core parameters, namely precursor concentration, solvent identity, and reaction temperature, to exploit the advantages of the HHTT ligand in terms of improving the size and degree of crystallinity of the resulting 2D MOF (Supplementary Table 1).

Reactions of HHTT with a variety of divalent metal ions in mixtures of *N,N*-dimethylformamide (DMF) and water produce a family of 2D π-conjugated MOFs, M_mHHTT_n ($m = 3$, $n = 2$ for Cu^{2+} and Ni^{2+}; $m = 6$, $n = 3$ for Co^{2+}, Mg^{2+}, Ni^{2+}; see Fig. 1c). Single crystals exhibiting rod- or plate-like morphology and ranging in size from 5 μm to 200 μm can be grown for all five materials, with the structural type correlated with the preferred geometry around the metal ion (Supplementary Table 1, Fig. 1d, Supplementary Fig. 7 and Supplementary Information). The high quality and relatively large size of the crystals facilitate atomic-resolution structural analysis by single-crystal X-ray diffraction (SXRD), continuous rotation electron diffraction (cRED) and high-resolution transmission electron microscopy (HRTEM).

Structural details of M_3HHTT_2 crystals

Metals that prefer square-planar coordination yield 2D honeycomb sheets with the formula M_3HHTT_2 ($M = Cu^{2+}$ or Ni^{2+}), which feature eclipsed packing and vacant pores. As a representative example, Cu_3HHTT_2 forms single crystals that present either as 5-μm-wide hexagonal plates or as 10-μm-wide hexagonal rods (Fig. 1d, Supplementary Fig. 7). The crystals are of sufficient size and quality to allow structural refinement by cRED with a resolution of ~1.5 Å (Fig. 2c, Supplementary Figs. 20–22). Cu^{2+} ions and two catechol units on neighbouring HHTT cores form square-planar $[CuO_4]$ secondary building units (SBUs). Each trigonal HHTT ligand is naturally surrounded by three SBUs to form infinite planar 2D sheets (Fig. 2a,b). These sheets stack in perfectly eclipsed AA fashion. Although the exact stacking sequences in other 2D conductive MOFs are unknown, perfectly eclipsed AA stacking is considered rare. Here, it likely results from the enhanced π-stacking interactions between HHTT cores in neighbouring sheets. A more convincing indication of the strong π-stacking in Cu_3HHTT_2 is the unusually small interlayer distance of 3.19 ± 0.02 Å, as determined by cRED. This interlayer distance is shorter than that in any other 2D MOF and is even shorter than the stacking distance of graphene sheets in natural graphite[28]. The stacked 2D sheets form 1D hexagonal pores with a diameter of 2.3 nm, which is in good agreement with the average pore size of 2.1 nm obtained by fitting a N_2 absorption isotherm to Cu_3HHTT_2 of an activated material (Supplementary Fig. 13). Fitting the N_2 adsorption isotherm of Cu_3HHTT_2 to the Brunauer–Emmett–Teller (BET) equation gives an apparent surface area of $1,360 \pm 20$ m² g⁻¹ (Supplementary Fig. 14). This value is considerably higher than those reported for other 2D conductive MOFs, and is in line with both a higher degree of crystallinity and the slightly larger pore size of this material[19].

The highly ordered nature of HHTT-based MOFs is also highlighted by near-atomic-resolution HRTEM down to 1.9 Å. This resolution is remarkable given the well-known beam sensitivity of similar materials[18,29–37]. The HRTEM images show that the crystals of Cu_3HHTT_2 exhibit long-range order across the whole crystallite and along all three crystallographic directions (Fig. 2k, Supplementary Fig. 54). Micrographs exploring the in-plane arrangement (Fig. 2d,e,g) show a well-resolved extended honeycomb framework (bright contrast) and pores (dark contrast) with a pore size of 2.1 nm. The simulated HRTEM image matches well with the averaged experimental image obtained for thick and thin crystals, and the thickness obtained from the image simulation is also consistent with the atomic force microscopy (AFM) results (Fig. 2f, Supplementary Figs. 52, 53 and 61). Micrographs exploring the stacking direction

(Fig. 2i) show atomically flat sheets with an interlayer spacing of 3.3 Å. Fast Fourier transform (FFT) of these images shows good agreement with eclipsed stacking between the sheets (Fig. 2c,d,i; for additional information on HRTEM, see Supplementary Figs. 46–54). Altogether, the HRTEM data are in excellent agreement with the more detailed structure derived from cRED and reveal important additional features that are not distinguishable with the latter. Thus, close examination of the crystal edges reveals termination by Cu^{2+} (and likely the coordinating solvent) rather than organic ligands (Supplementary Fig. 46c,d), which is probably due to the excess stoichiometry of Cu^{2+} during synthesis. Remarkably, the HRTEM data reveal isolated in-plane moiré superlattices (Supplementary Figs. 54 and 57) from twisted overlapping neighbouring sheets, suggesting that the single crystals are potentially exfoliatable. Moiré superlattices have recently attracted attention owing to their ability to modulate the electronic band structures of the underlying single sheets in graphene and other 2D van der Waals materials[38]. The large crystals of HHTT-based materials may provide interesting opportunities to explore similar effects in MOFs in the future.

Guest molecule inclusion in crystals of M_6HHTT_3

Metal ions that do not easily accommodate a square-planar geometry but instead prefer octahedral coordination form similar SBUs with two equatorially oriented catechol groups and also feature axially coordinated water molecules to give materials with the formula $[M_3(HHTT)_2(H_2O)_6 \cdot M_3(HHTT)(H_2O)_{12}]$[1] ($M_6HHTT_3$, $M = Co^{2+}$, Mg^{2+} and Ni^{2+}) (Fig. 3a). Despite coordination to only one catechol group, the cobalt centres in the guest molecules share a similar $[CoO_6]$ SBU. As a representative example, Co_6HHTT_3 can be grown as large hexagonal rods, approximately 20 μm in diameter and 200 μm in length, which are amenable for single-crystal X-ray diffraction analysis (Fig. 1d, Supplementary Fig. 38). These data reveal that the axial molecules disrupt the π-stacking observed in Cu_3HHTT_2, increase the interlayer spacing to 3.2–3.3 Å (Fig. 3b) and cause slippage of the 2D honeycomb M_3HHTT_2 sheets into a staggered ABC packing motif (Fig. 3c). The staggered packing eliminates the 1D pores, and the remaining open space is occupied by well-defined $Co_3(HHTT)(H_2O)_{12}$ clusters centred in the hexagonal pockets defined by the 2D sheets (Fig. 3a,c–f). These molecular clusters have no direct bonding with the extended framework sheets (Fig. 3a) but engage in extensive hydrogen bonding interactions with neighbouring MOF layers (Fig. 3c). As with Cu_3HHTT_2, HRTEM analysis of Co_6HHTT_3 confirms long-range ordering and reveals honeycomb lattice fringes that extend throughout the crystal lattice, with lattice periodicities resolved down to 4.6 Å (Fig. 3g, Supplementary Fig. 56). Contrast analysis of the HRTEM data at high magnification further reveals the in-pore Co_3 clusters that are clearly distinguishable from the extended lattices (Fig. 3h). Surprisingly, lattice fringes that extend along the length of the crystallographic c axis exhibit alternating high- and low-contrast fringes spaced at 1.05 nm (Fig. 3i,j). The emergence of high- and low-contrast fringes in Co_6HHTT_3, not observed in Cu_3HHTT_2, also confirms the presence of staggered in-pore clusters (Fig. 2h–k). Mg_6HHTT_3 presents structural features that are essentially identical to those of the Co analogue, as expected for Mg^{2+} ions, which prefer octahedral coordination (Supplementary Figs. 30–32 and 57).

Owing to its ability to form both square-planar and octahedral complexes with medium-weak oxygen donor ligands, Ni^{2+} showcases the crystal growth and product selectivity control facilitated by ligands with the characteristics of HHTT. We surmised that in the $DMF:H_2O$ solvent continuum, DMF would be more effective in disrupting the strong π-stacking between the sheets than water (Supplementary Fig. 45)[39]. Indeed, the reaction between Ni^{2+} and HHTT in the presence of DMF (Supplementary Table 1) yields large crystals of Ni_3HHTT_2, whose structure, revealed by cRED down to a resolution of 1.5 Å, is identical to that of Cu_3HHTT_2 and retains
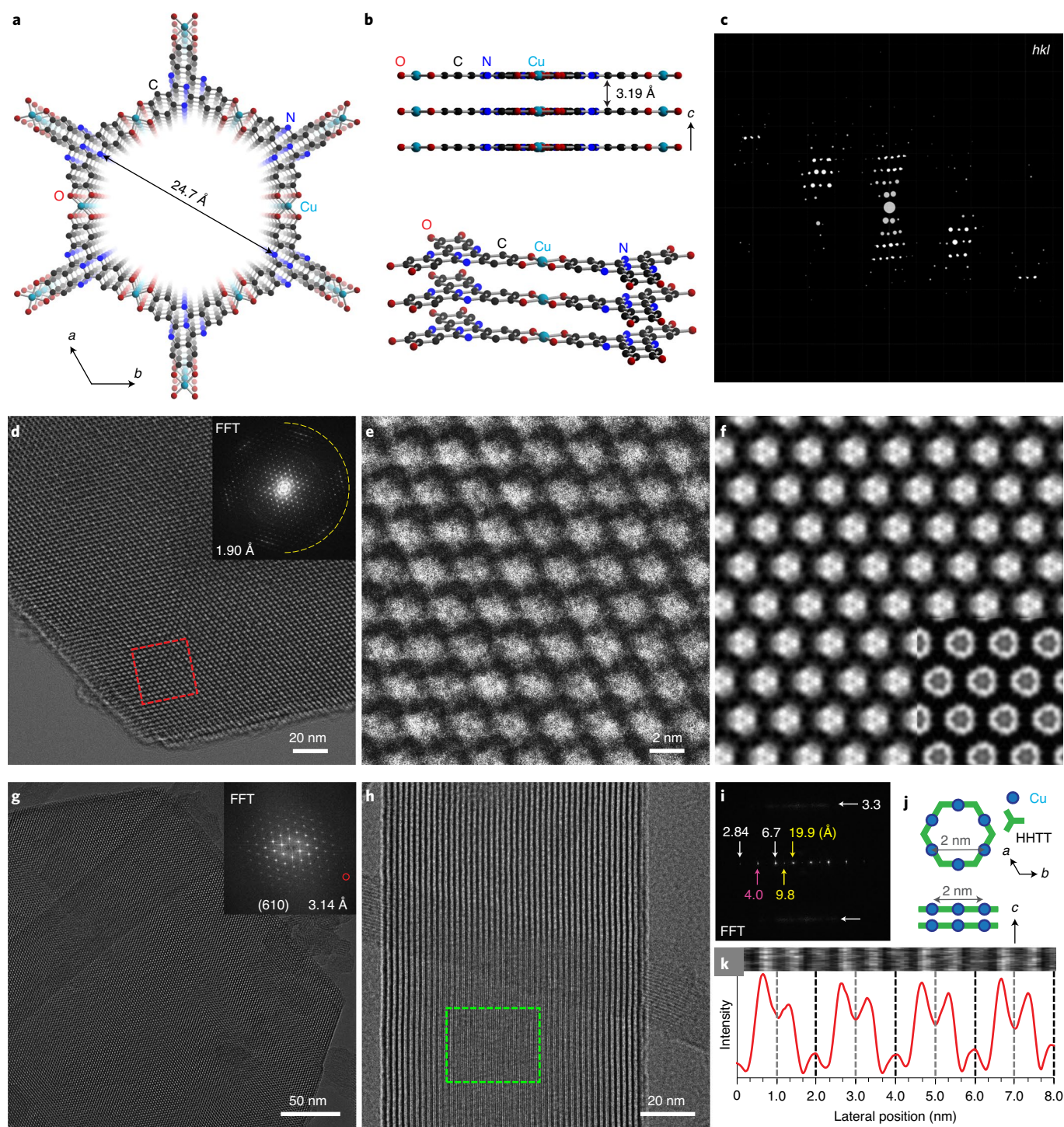
Fig. 2 | Single-crystal structure of Cu₃HHTT₂ derived from cRED and HRTEM. a, A portion of the crystal structure along the *c* direction. **b**, Views parallel to the *ab* plane. Hydrogen atoms are omitted for clarity. **c**, 3D reciprocal lattices of a Cu₃HHTT₂ rod with a maximum resolution of 1.5 Å (*hkl* corresponds to reciprocal space indices). **d**, Cryo-EM image of a Cu₃HHTT₂ plate (inset: FFT). **e**, High-magnification image from the red square in **d**. **f**, Averaged experimental image (inset: simulated HRTEM image). **g**, Low-magnification image of ~1 µm Cu₃HHTT₂ plate (inset: FFT of the micrograph). **h**, HRTEM image of a Cu₃HHTT₂ rod imaged normal to the *c* direction. **i**, FFT of the image from the green square in **h**, evidencing the eclipsed stacking in the reciprocal lattice. **j**, Schematic of Cu₃HHTT₂ structure to illustrate imaging directions. **k**, Average intensity in the *c*-direction measured along the *a*-direction from the image in **h**.

the close interlayer spacing of 3.19 Å (Supplementary Figs. 18, 19, 23–27 and 55). In the absence of DMF, Ni^{2+} and HHTT form $[Ni_3(HHTT)_2(H_2O)_6 \cdot Ni_3(HHTT)(H_2O)_{12}]$ (Ni_6HHTT_3), a dense network that is essentially identical to Co_6HHTT_3 (Supplementary Figs. 28, 29, 33–37 and 58), with only small variations stemming

from the difference in interlayer interactions owing to hydrogen bonding and the solvent content. The behaviour of Ni^{2+} in this system establishes the identity of the metal ion as an important variable in defining the stacking sequence in 2D conductive MOFs in addition to the molecular and electronic structure of the ligand.
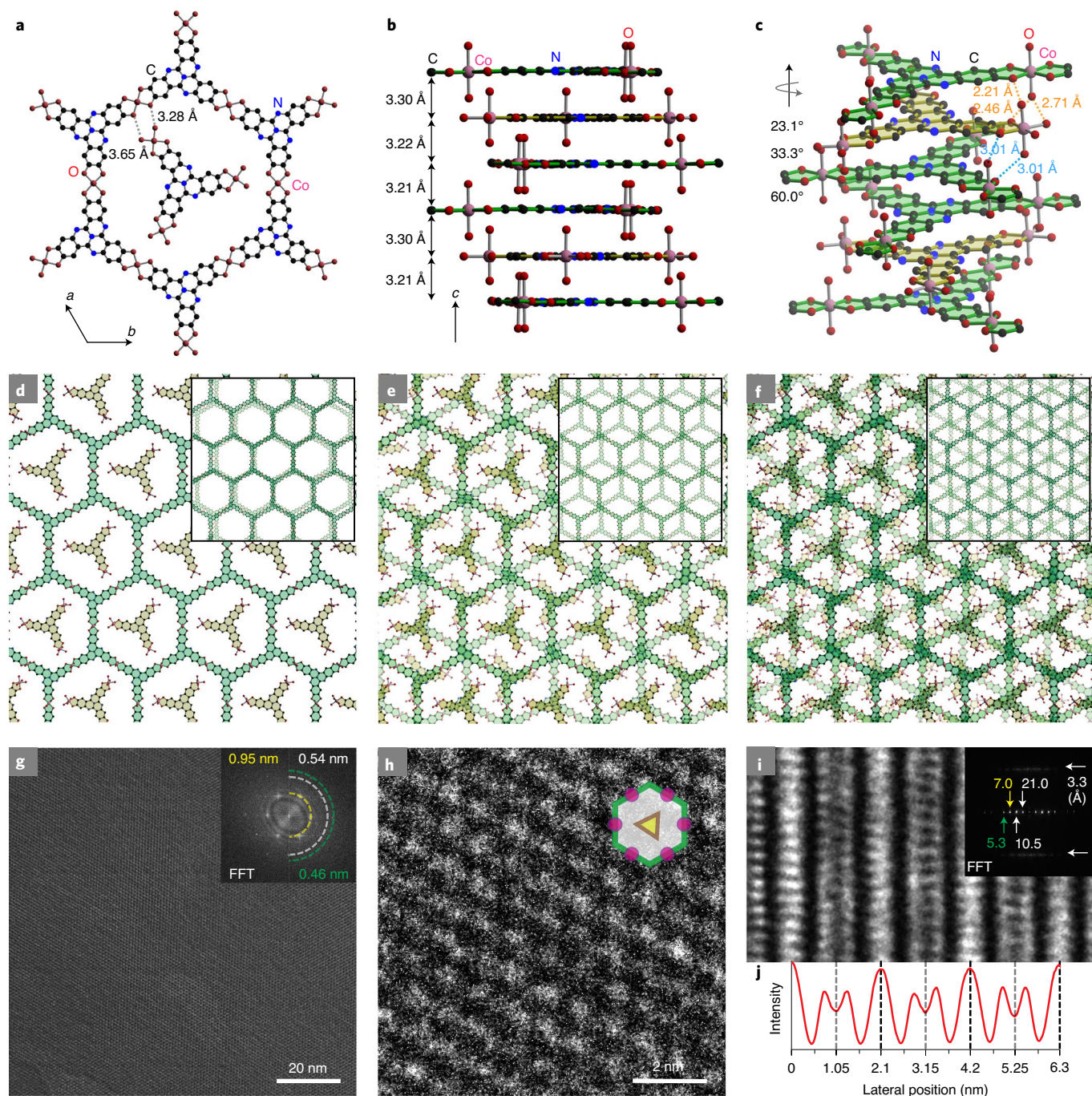
Fig. 3 | Single-crystal structure of Co$_6$HHTT$_3$ derived from SXRD and HRTEM. a, Portion of the crystal structure viewed along the *c* direction. The long O–O distances suggest that no hydrogen bonds are formed between the molecular clusters and the Co$_3$HHTT$_2$ sheets. **b**, View along the *ab* plane showing an (ABC)$_n$ triple sheet stacking motif. **c**, Spatial relationships between molecular and extended Co-HHTT units. The sheets and molecular units are indicated in green and yellow, respectively. The interlayer hydrogen bonds are represented by orange and blue dashed lines. **d**–**f**, Structural representations of single, double and triple layers of Co$_6$HHTT$_3$. The insets in **d**, **e** and **f** show views normal to the two closest A layers, one AB layer set, and an ABC stack, respectively. All guest molecules are omitted for clarity. **g**, HRTEM images of a Co$_6$HHTT$_3$ plate with long-range lattice fringes extending across the entire crystal. Inset: FFT of the micrograph. **h**, High-magnification micrograph where intra-pore clusters are visible, as indicated by a primary hexagonal periodicity of 0.95 nm, approximately half of that of Cu$_3$HHTT$_2$, which does not contain guest clusters. **i**, HRTEM image of a Co$_6$HHTT$_3$ rod imaged normal to the *c* axis. Inset: FFT from the image in **i**, revealing an interlayer stacking of ~3.3 Å. **j**, Average intensity of the image in **i**, integrated down the *c* direction and measured across the *a* direction (lateral position, left to right).

Anisotropic electrical transport in 2D MOF single crystals

The large single crystals of MOFs made from HHTT provide a unique opportunity for understanding anisotropic charge transport in this class of materials. Four-probe devices were fabricated by electron-beam lithography from large hexagonal plates or hexagonal rods of different materials to probe in-plane and out-of-plane electrical transport, respectively (Fig. 4a,b, Supplementary Figs. 59–66). The room temperature conductivity values, summarized in Fig. 4c, reveal several surprising trends that are qualitatively explained well by the structural data. First, the in-plane conductivity
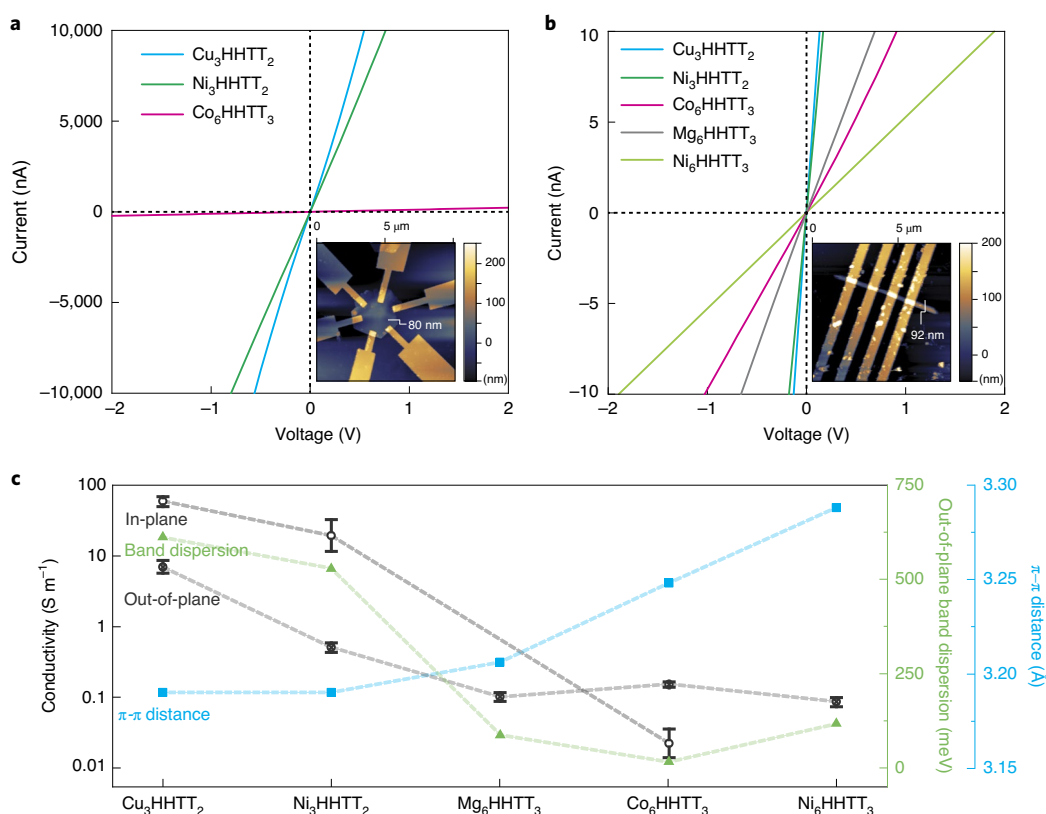
Fig. 4 | Electrical transport data for 2D M_mHHTT_n MOFs. a, In-plane van der Pauw *I–V* curves measured from electron-beam devices made from hexagonal single-crystal plates. **b**, Out-of-plane four-probe *I–V* curves measured from electron-beam devices made from single-crystal rods. In both **a** and **b**, the linearity of the *I–V* plots confirms ohmic behaviour, with the slope variation depending on the crystal orientation and MOF identity. The insets show representative AFM images and the thicknesses of the in-plane and out-of-plane Cu_3HHTT_2 devices. **c**, Single-crystal conductivity data (in-plane and out-of-plane), out-of-plane band dispersion and π-stacking distance of 2D M_mHHTT_n MOFs (average and standard deviation obtained from 10 devices). The gradient to the right of the graph separates the three dense HHTT-based analogues.

of the porous, eclipsed phase M_3HHTT_2 (M = Cu^{2+} or Ni^{2+}) is expectedly higher than its out-of-plane conductivity, whereas the dense staggered phase Co_6HHTT_3 shows higher out-of-plane conductivity. Notably, the in-plane conductivity of ~100 S m^{-1} observed for Cu_3HHTT_2 compares favourably with the highest conductivity reported for any MOF[40]. We surmise that the planar Co_3 clusters residing within the latter contribute towards transport normal to the 2D sheets and potentially also impede transport within the sheet through greater phonon scattering or narrower band dispersion (Fig. 4c). Second, the eclipsed phases are more conductive than the staggered phases in either crystallographic direction. This is most evident in the two phases made from Ni^{2+} (Ni_3HHTT_2 is approximately 10 times more conductive than Ni_6HHTT_3) and is clearly correlated with the much closer stacking distance in the former. More generally, the out-of-plane conductivity for all MOFs is inversely related to the interlayer π–π distances, with the exception of Mg_6HHTT_3, where the metal-based *d* orbital is absent. Finally, within the more conductive eclipsed group M_3HHTT_2, the Cu analogue is more conductive than the Ni analogue in both directions. Conversely, within the dense staggered phase M_6HHTT_3 (M = Mg^{2+}, Co^{2+} and Ni^{2+}), the out-of-plane conductivities are nearly identical for all three materials.

Density functional theory calculations, exploring the band structure as well as the charge and spin distribution for each M_mHHTT_n MOF, provide deeper insights into the qualitative trends observed for conductivity data. The calculations assumed that all metals are in the formal oxidation state +2, as confirmed by investigations of their absorption edge positions via X-ray absorption near-edge

spectroscopy (XANES) and X-ray photoelectron spectroscopy (XPS) (Supplementary Figs. 39–44 and 68–70), with the charge on Co and Cu further supported by electron paramagnetic resonance (EPR) measurements (Supplementary Fig. 67a,b). Based on charge neutrality, the HHTT ligands within the extended sheets were assumed to be triply oxidized (that is, HHTT^{3-}), a formal charge assignment that is further supported by the presence of an organic radical in EPR (Supplementary Fig. 67). Conversely, the HHTT ligands of $M_3(HHTT)(H_2O)_{12}$ clusters centred in the hexagonal pockets were assumed to be fully reduced (that is, HHTT^{6-}), supported by the elemental analysis data[1]. The band structure diagrams and corresponding density of states (DOS) plots reveal a positive correlation between the proximity of occupied metal-based *d*-states near the Fermi level and the in-plane conductivity (Supplementary Figs. 71 and 72). The eclipsed phase M_3HHTT_2 (M = Cu^{2+}, Ni^{2+}) has widely dispersed bands consisting of orbitals from both metal ions and ligands at the Fermi level in both in-plane and out-of-plane directions, whereas the dense phase M_6HHTT_3 (M = Co^{2+}, Mg^{2+}, Ni^{2+}) has relatively narrow bands at the Fermi level. This significant difference indicates that the high conductivity observed in the porous phase is a result of effective orbital mixing. In the in-plane direction, the energy matching between the orbitals of square-planar Cu^{2+} or Ni^{2+} ions and those of the radical-state ligands leads to in-plane π-conjugation; in the out-of-plane direction, the strong interlayer π–π interaction and the lack of steric hindrance from axial ligands give rise to a dense packing motif. Both of these factors result in well-mixed orbitals, which translate to dispersed bands and efficient charge transport. By contrast, in the dense staggered phase, the guest monomer interpenetration and

the coordinating axial solvent interfere with the in-plane π-conjugation and interlayer packing, respectively, giving rise to ineffective orbital mixing, narrow bands and consequently inefficient charge transport in both directions. The contrast between the band diagrams of the two structure types also rationalizes their different trends for anisotropic transport and the important influence of metal ions on conductivity. In the eclipsed phase M_3HHTT_2, the in-plane charge transport is highly efficient owing to effective π-conjugation, resulting in higher in-plane conductivity than out-of-plane conductivity. The metal ions participate in charge transport and contribute charge carriers, thus significantly affecting conductivity and resulting in higher conductivity in Cu_3HHTT_2 with d^9-Cu^{2+} ions than that in Ni_3HHTT_2 with d^8-Ni^{2+} ions. On the other hand, in the dense phase, interlayer charge hopping is dominant owing to the absence of in-plane π-conjugation, which gives rise to the opposite anisotropy. Indeed, charge transport in the dense staggered phase is mainly ligand based. Because there is little contribution from metal ions, the out-of-plane conductivities among the three analogues in this phase are nearly identical. Overall, the experimental and theoretical studies reveal the decisive influence of the extent of π-conjugation and the packing motif on electrical conduction in 2D π-conjugated MOFs, highlighting a design principle for future development of this class of materials.

Outlook

We presented atomically precise structural data for an important class of conductive MOFs and established clear correlations between structure and transport properties in these materials. Single-crystal devices reveal anisotropic conductivity trends that can only be explained with the aid of high-resolution structural data. The structure–conductivity relationships elaborated herein provide a blueprint for a well-guided approach towards the design and development of porous, conductive 2D MOFs.

Online content

Any methods, additional references, Nature Research reporting summaries, source data, extended data, supplementary information, acknowledgements, peer review information; details of author contributions and competing interests; and statements of data and code availability are available at https://doi.org/10.1038/s41563-020-00847-7.

References

1. Hmadeh, M. et al. New porous crystals of extended metal-catecholates. *Chem. Mater.* **24**, 3511–3513 (2012).
2. Sheberla, D. et al. High electrical conductivity in Ni₃(2,3,6,7,10,11-hexaiminotriphenylene)₂, a semiconducting metal–organic graphene analogue. *J. Am. Chem. Soc.* **136**, 8859–8862 (2014).
3. Dong, R. et al. High-mobility band-like charge transport in a semiconducting two-dimensional metal–organic framework. *Nat. Mater.* **17**, 1027–1032 (2018).
4. Kambe, T. et al. π-Conjugated nickel bis(dithiolene) complex nanosheet. *J. Am. Chem. Soc.* **135**, 2462–2465 (2013).
5. Talin, A. A. et al. Tunable electrical conductivity in metal-organic framework thin-film devices. *Science* **343**, 66–69 (2014).
6. Aubrey, M. L. et al. Electron delocalization and charge mobility as a function of reduction in a metal–organic framework. *Nat. Mater.* **17**, 625–632 (2018).
7. Nam, K. W. et al. Conductive 2D metal-organic framework for high-performance cathodes in aqueous rechargeable zinc batteries. *Nat. Commun.* **10**, 4948 (2019).
8. Wada, K., Sakaushi, K., Sasaki, S. & Nishihara, H. Multielectron-transfer-based rechargeable energy storage of two-dimensional coordination frameworks with non-innocent ligands. *Angew. Chem. Int. Ed.* **57**, 8886–8890 (2018).
9. Pomerantseva, E., Bonaccorso, F., Feng, X., Cui, Y. & Gogotsi, Y. Energy storage: the future enabled by nanomaterials. *Science* **366**, eaan8285 (2019).
10. Sheberla, D. et al. Conductive MOF electrodes for stable supercapacitors with high areal capacitance. *Nat. Mater.* **16**, 220–224 (2017).
11. Wang, H., Zhu, Q.-L., Zou, R. & Xu, Q. Metal-organic frameworks for energy applications. *Chem* **2**, 52–80 (2017).
12. Feng, D. et al. Robust and conductive two-dimensional metal–organic frameworks with exceptionally high volumetric and areal capacitance. *Nat. Energy* **3**, 30–36 (2018).
13. Miner, E. M. et al. Electrochemical oxygen reduction catalysed by Ni₃(hexaiminotriphenylene)₂. *Nat. Commun.* **7**, 10942 (2016).
14. Stassen, I. et al. An updated roadmap for the integration of metal–organic frameworks with electronic devices and chemical sensors. *Chem. Soc. Rev.* **46**, 3185–3241 (2017).
15. Evans, A. M. et al. Seeded growth of single-crystal two-dimensional covalent organic frameworks. *Science* **361**, 52–57 (2018).
16. Ma, T. et al. Single-crystal X-ray diffraction structures of covalent organic frameworks. *Science* **361**, 48–52 (2018).
17. Zhao, M. et al. Two-dimensional metal–organic framework nanosheets: synthesis and applications. *Chem. Soc. Rev.* **47**, 6267–6295 (2018).
18. Zhong, Y. et al. Wafer-scale synthesis of monolayer two-dimensional porphyrin polymers for hybrid superlattices. *Science* **9385**, 1379–1384 (2019).
19. Sun, L., Campbell, M. G. & Dincă, M. Electrically conductive porous metal–organic frameworks. *Angew. Chem. Int. Ed.* **55**, 3566–3579 (2016).
20. Dou, J.-H. et al. Signature of metallic behavior in the metal–organic frameworks M₃(hexaiminobenzene)₂ (M = Ni, Cu). *J. Am. Chem. Soc.* **139**, 13608–13611 (2017).
21. Day, R. W. et al. Single crystals of electrically conductive two-dimensional metal–organic frameworks: structural and electrical transport properties. *ACS Cent. Sci.* **5**, 1959–1964 (2019).
22. Miao, Q. Ten years of N-heteropentacenes as semiconductors for organic thin-film transistors. *Adv. Mater.* **26**, 5541–5549 (2014).
23. Wang, C., Dong, H., Jiang, L. & Hu, W. Organic semiconductor crystals. *Chem. Soc. Rev.* **47**, 422–500 (2018).
24. Watson, M. D., Fechtenkötter, A. & Müllen, K. Big is beautiful - 'Aromaticity' revisited from the viewpoint of macromolecular and supramolecular benzene chemistry. *Chem. Rev.* **101**, 1267–1300 (2001).
25. Okamoto, T. et al. Robust, high-performance n-type organic semiconductors. *Sci. Adv.* **6**, eaaz0632 (2020).
26. Rieth, A. J., Wright, A. M. & Dincă, M. Kinetic stability of metal–organic frameworks for corrosive and coordinating gas capture. *Nat. Rev. Mater.* **4**, 708–725 (2019).
27. Van Vleet, M. J., Weng, T., Li, X. & Schmidt, J. R. In situ, time-resolved, and mechanistic studies of metal–organic framework nucleation and growth. *Chem. Rev.* **118**, 3681–3721 (2018).
28. Skorupskii, G. et al. Efficient and tunable one-dimensional charge transport in layered lanthanide metal–organic frameworks. *Nat. Chem.* **12**, 131–136 (2020).
29. Zhang, D. et al. Atomic-resolution transmission electron microscopy of electron beam-sensitive crystalline materials. *Science* **359**, 675–679 (2018).
30. Liu, K. et al. On-water surface synthesis of crystalline, few-layer two-dimensional polymers assisted by surfactant monolayers. *Nat. Chem.* **11**, 994–1000 (2019).
31. Lebedev, O. I., Millange, F., Serre, C., Van Tendeloo, G. & Férey, G. First direct imaging of giant pores of the metal–organic framework MIL-101. *Chem. Mater.* **17**, 6525–6527 (2005).
32. Wiktor, C., Meledina, M., Turner, S., Lebedev, O. I. & Fischer, R. A. Transmission electron microscopy on metal–organic frameworks - a review. *J. Mater. Chem. A* **5**, 14969–14989 (2017).
33. Liu, L. et al. Imaging defects and their evolution in a metal–organic framework at sub-unit-cell resolution. *Nat. Chem.* **11**, 622–628 (2019).
34. Li, Y. et al. Cryo-EM structures of atomic surfaces and host-guest chemistry in metal-organic frameworks. *Matter* **1**, 428–438 (2019).
35. Mayoral, A., Mahugo, R., Sánchez-Sánchez, M. & Díaz, I. Cs-corrected STEM imaging of both pure and silver-supported metal-organic framework MIL-100(Fe). *ChemCatChem* **9**, 3497–3502 (2017).
36. Shen, B., Chen, X., Shen, K., Xiong, H. & Wei, F. Imaging the node-linker coordination in the bulk and local structures of metal-organic frameworks. *Nat. Commun.* **11**, 2692 (2020).
37. Zhou, Y. et al. Local structure evolvement in MOF single crystals unveiled by scanning transmission electron microscopy. *Chem. Mater.* **32**, 4966–4972 (2020).
38. Cao, Y. et al. Unconventional superconductivity in magic-angle graphene superlattices. *Nature* **556**, 43–50 (2018).
39. Hestand, N. J. & Spano, F. C. Expanded theory of H- and J-molecular aggregates: the effects of vibronic coupling and intermolecular charge transfer. *Chem. Rev.* **118**, 7069–7163 (2018).
40. Xie, L. S., Skorupskii, G. & Dincă, M. Electrically conductive metal–organic frameworks. *Chem. Rev.* **120**, 8536–8580 (2020).

Methods

Synthesis of M_mHHTT_n MOFs. Solutions of HHTT and metal salt precursors ($CuSO_4 \cdot 5H_2O$ for $M = Cu^{2+}$; $M(OAc)_2 \cdot 4H_2O$ for $M = Ni^{2+}$, Co^{2+}, Mg^{2+}) were mixed in air and sealed at room temperature inside 20 ml Teflon sleeves of Parr bombs (Cu_3HHTT_2, Ni_3HHTT_2, Co_6HHTT_3, Mg_6HHTT_3 rods) or 20 ml scintillation vials (all other MOFs). Aqueous solutions of anhydrous sodium acetate were further added to the mixture for the synthesis of Mg_6HHTT_3. After heating at elevated temperature for 12 h, a black precipitate formed from the initial cloudy red mixture. The final products were isolated by centrifugation, washed extensively with a series of solvents with decreasing polarity and dried under vacuum. The detailed procedures and elemental analysis results are presented in the Supplementary Information.

Single-crystal X-ray diffraction. The synchrotron SXRD data were collected at beamlines BL17B1 and BL19U1 of the Shanghai Synchrotron Radiation Facility (SSRF) with $\lambda = 0.9840$ and 0.82654 Å, respectively. All the datasets of single-crystal MOFs were collected at 100 K, and the data were accordingly processed with CrysAlisPro (version 1.171.37.35), HKL3000 and APEXII software packages, depending on the instrument setup. The structure solution and refinement were carried out using SHELXT (ref. [41]) and SHELXL (ref. [42]). Two datasets of Co_6HHTT_3 and four datasets of Mg_6HHTT_3 were merged to increase the completeness for the refinement. According to the intensity statistics table for the whole dataset (PRP file), the resolutions of Co_6HHTT_3 and Mg_6HHTT_3 were cut off to 0.90 Å and 1.05 Å, respectively. To deduct the contribution of diffraction from the disordered guest molecules in the pores, PLATON SQUEEZE[43] procedures were conducted during the refinement. The structures were refined anisotropically.

3D electron diffraction data collection. 3D electron diffraction data were collected under cryo-condition (95 K) using the cRED method implemented in Instamatics (ref. [44,45]). All the datasets were collected using a JEOL JEM2100 TEM (LaB_6 filament equipped with Amsterdam Scientific Instruments Timepix camera) operating at 200 kV. During the data collection, the goniometer was rotated continuously while the selected area ED patterns were captured from the crystal simultaneously. The reciprocal space reconstruction was carried out using REDp (ref. [46]), and the reflection intensity extraction was conducted using X-ray Detector Software (XDS) (ref. [47]). Using the intensities obtained from the 3D ED data, the structures were solved ab initio using SHELXT (ref. [41]).

High-resolution transmission electron microscopy. HRTEM images were obtained via a spherical-aberration-corrected FEI Titan 80-300, operated at an accelerating voltage of 300 kV and equipped with a Gatan K2 in situ direct electron detector at Center for Functional Nanomaterials (CFN), Brookhaven National Laboratory (BNL). MOF samples dispersed in methanol were dropcasted onto Cu TEM grids. The TEM dose rate was maintained between 4.8 and 18.7 e^- per Å^2 per s. We note that no damage to the MOF structures was detected during brief exposures under these dose conditions; however, higher doses would cause significant and rapid structural damage. All the images were acquired using Digital Micrograph 4.0 with an exposure time of 0.3 s (~1.5–5.6 e^- per Å^2 cumulative dose per image), with focusing done adjacent to the region imaged to minimize beam exposure prior to image acquisition (standard low dose imaging protocols). Analyses of the raw HRTEM data (.dm4), including FFT and intensity profile analysis, were performed using FIJI ImageJ (https://imagej.net/Fiji/). Cryo-EM images of Cu_3HHTT_2 (Fig. 2d,e) were obtained using a Titan Krios G3i transmission electron microscope operated at an accelerating voltage of 300 kV with a Gatan BioQuantum-K3 energy-filtered detector. The images in Supplementary Fig. 53 were obtained using a Talos Arctica G2 transmission electron microscope operated at an accelerating voltage of 200 kV with a Falcon3EC direct electron detector.

Device fabrication and characterization. Samples of rods or plates were suspended in hexane and drop-casted onto Si/SiO_2 substrates having pre-patterned marks for optical alignment and registration. The samples were then annealed at 338.15 K for 12 h in a vacuum oven. Two layers of MMA and one layer of PMMA were coated onto the chips, and the layers were baked at 358.15 K for 5 min in a vacuum oven. Electron-beam lithography at 30 kV was performed to pattern the contacts, and 5 nm Ti/250 nm Au contacts were evaporated using an electron-beam evaporator. The sample device substrates were subsequently soaked in acetone for a 24 h lift-off process.

All electrical measurements were performed in dark conditions at room temperature under vacuum (10^{-5} mbar). Van der Pauw or four-probe configurations were adopted for plate- or rod-like crystals to minimize the effect of contact resistance[40,48]. For van der Pauw measurements (Fig. 4a), four probes were connected to a source meter (Keithley 2450) through triax cables (Keithley 7078-TRX-10). I–V curves were obtained by scanning the current from $-10 \mu A$ to $10 \mu A$ with a step size of 0.5 μA, speed of 5 number of power line circles (NPLC) and delay of 2 ms; the voltage was measured at each step (for Co_6HHTT_3, -20 nA to 20 nA with a step size of 0.5 nA). For the detailed van der Pauw calculations, see ref. [48]. For four-probe rod measurements (Fig. 4b), linear I–V curves were obtained by

supplying current from -10 nA to 10 nA with a step size of 0.5 nA (Keithley 2450). The current was supplied through the outer two probes, while the voltage was measured through the inner two probes. At least 10 plates and rods of each MOF were measured.

Computational methods. Quantum chemical simulations were performed using Vienna Ab initio Simulation Package (VASP) and Gaussian09 for periodic and single molecule models, respectively. In both cases, the structures were obtained experimentally and geometrically equilibrated using the functionals and basis sets detailed in the Supplementary Information. A pure GGA functional was used to compute the electronic band structure of these metallic materials, while a hybrid functional based on GGA was used to recover more accurate pK_a estimates for single molecular linkers. The full computational details are presented in the Supplementary Information.

Data availability

The crystallographic information has been deposited in the Cambridge Crystallographic Data Centre (CCDC) under accession codes 2031852–2031856. All other data supporting the findings of this study are available within the article and its Supplementary Information.

References

41. Sheldrick, G. M. SHELXT - Integrated space-group and crystal-structure determination. *Acta Crystallogr. Sect. A Found. Crystallogr.* **71**, 3–8 (2015).
42. Sheldrick, G. M. Crystal structure refinement with SHELXL. *Acta Crystallogr. Sect. C. Struct. Chem.* **71**, 3–8 (2015).
43. Spek, A. L. PLATON SQUEEZE: a tool for the calculation of the disordered solvent contribution to the calculated structure factors. *Acta Crystallogr. Sect. C. Struct. Chem.* **71**, 9–18 (2015).
44. Wang, Y. et al. Elucidation of the elusive structure and formula of the active pharmaceutical ingredient bismuth subgallate by continuous rotation electron diffraction. *Chem. Commun.* **53**, 7018–7021 (2017).
45. Smeets, S., Zou, X. & Wan, W. Serial electron crystallography for structure determination and phase analysis of nanocrystalline materials. *J. Appl. Crystallogr.* **51**, 1262–1273 (2018).
46. Wan, W., Sun, J., Su, J., Hovmöller, S. & Zou, X. Three-dimensional rotation electron diffraction: software RED for automated data collection and data processing. *J. Appl. Crystallogr.* **46**, 1863–1873 (2013).
47. Kabsch, W. et al. XDS. *Acta Crystallogr. Sect. D. Biol. Crystallogr.* **66**, 125–132 (2010).
48. Sun, L., Park, S. S., Sheberla, D. & Dincă, M. Measuring and reporting electrical conductivity in metal–organic frameworks: $Cd_2(TTFTB)$ as a case study. *J. Am. Chem. Soc.* **138**, 14772–14782 (2016).

Author contributions

J.-H.D., J.S. and M.D. conceived the idea and designed the experiments. J.-H.D. performed and interpreted the synthesis, crystal growth, HRTEM (cryo-EM) experiments and electron-beam device fabrication. M.Q.A. performed and interpreted the AFM and device measurements. Y.L., J.L. and W.Z. carried out the crystallographic studies. J.L.M., M.C.Y. and C.H.H. performed and interpreted the pK_a and DFT calculations. N.J.L. and J.T.M. performed and interpreted the XANES measurement.

Additional information